JOM, Vol. 76, No. 10, 2024
https://doi.org/10.1007/s11837-024-06786-x

TECHNICAL ARTICLE

Effect of Nano Reinforcements on the Hardness and Corrosion Resistance of Hybrid Composites

T. SARITHNAIDU[1,2] and KAMBAGOWNI VENKATASUBBAIAH[1]

1.—Department of Mechanical Engineering, Andhra University, Visakhapatnam 530003, India.
3.—e-mail: chukkasaritha11@gmail.com

This study investigated the ability of an aluminium 6351 matrix strengthened with a combination of nano-ceramic particulates to resist corrosion and mechanical characteristics while varying the nano-zirconia weight percent. To create the composite material, nano-zirconium dioxide particles were added in increments of 3% (ranging from 3 to 9 wt.%) to the AA6351-nanoSiC (5 wt.%) composite using powder metallurgy. To assess the effect of incorporating nano-zirconium dioxide reinforcement on the corrosion behaviour of the composite material, we conducted electrochemical polarisation measurements in a 3.5% sodium chloride solution and hardness by Vickers hardness. The study demonstrated that the addition of greater quantities of nano-zirconium dioxide (ZrO_2) particles to an aluminium alloy with a nano-silicon carbide (SiC) matrix resulted in an enhancement of its corrosion resistance. Quantitative analysis from microscopy data demonstrated a uniform distribution of reinforcing particles within the aluminium matrix, with minimal deviation from an even dispersion. Adding ZrO_2 nanoparticles to AA6351-SiC composites significantly boosted microhardness, peaking at 144.3 HV with 9 wt.% ZrO_2 content. These findings suggest that the incorporation of nano-zirconium dioxide particles in the aluminium alloy has the potential to improve its hardness and corrosion resistance, which could be valuable for a wide range of applications.

Abbreviations

AA	Aluminium alloy
AMC	Aluminium matrix composite
ASTM	American Society for Testing and Materials
BN	Boron nitride
BPR	Ball to powder ratio
CR	Corrosion rate (mm/year or mils per year)
E_{corr}	Corrosion potential
EDS	Energy-dispersive spectroscopy
EIS	Electrochemical impedance spectroscopy
HAMMC	Hybrid aluminium metal matrix composite
HANMMC	Hybrid aluminium nano-metal matrix composite
I_{corr}	Corrosion current density
JCPDS	Joint Committee on Powder Diffraction Standards
ICDD	International Centre for Diffraction Data
MMC	Metal matrix composite
OA	Orthogonal array
OCP	Open circuit potential
PM	Powder metallurgy
R_p	Polarization resistance
SEM	Scanning electron microscope
Si_3N_4	Silicon nitride
SiC	Silicon carbide
TEM	Transmission electron microscope
XRD	X-ray diffraction
ZrB_2	Zirconium diboride
ZrO_2	Zirconium dioxide or zirconia
β_a	Anodic slope (volts/decade)
β_c	Cathodic slope (volts/decade)

(Received March 30, 2024; accepted July 17, 2024;

INTRODUCTION

The desire to expand the range of applications for metals and alloys, particularly lightweight metals such as aluminium, magnesium, and titanium, has driven the development of improvements in these materials. These improvements are aimed at achieving higher levels of efficiency in their use, which can lead to their adoption in a broader range of applications.[1] Indeed, composites of aluminium alloy hold significant value as materials with diverse potential applications. Their versatility makes them suitable for various industries, including automotive, marine, aerospace, and offshore structures.[2] They are also used in a limited capacity for pressure vessels. aircraft, helicopters, and spacecraft.[3,4]

In recent times, metal matrix composites (aluminium) have generated increasing interest due to their ability to provide a broad spectrum of beneficial properties, such as good thermal stability and corrosion resistance, high strength, lower density and wear rate, and low production cost.[5] The structural and mechanical behaviour of aluminium metal matrix composites is greatly influenced by multiple factors, encompassing the arrangement and distribution of the reinforcing particles, as well as the production techniques applied, including stir casting, squeeze casting, ultrasonic-assisted stir casting, and powder metallurgy.[6,7] The use of particulate reinforcements is highly favoured because of their ability to reduce the particle size from micro- to nanoscale, resulting in improved morphological, physical, and mechanical properties. A wide range of materials, including Al_2O_3,[8] WC, graphite,[9] MWCNT, SiC,[10,11] AlN, B_4C,[12] TiC,[13,14] TiB_2,[15] fly ash,[16] ZrO_2,[17] ZrB_2, and Si_3N_4, is frequently utilized as reinforcement to enhance the mechanical properties of the base material.

Powder metallurgy is a highly favoured fabrication technique for AMCs because of its capability to produce products with near-net-like shapes and achieve a reasonable degree of reinforcing homogeneity in the composite material. This technique has gained significant interest because it helps reduce pricey manufacturing operations, making the production process cost-effective.[17] Hybrid composites, which consist of a combination of micro- and nano-sized or nano-nano-sized particles, have gained attention in scientific studies as a better alternative to mono-reinforced composites because of their superior physio-mechanical characteristics.[18] In their study, Thiagarajan et al.[19] examined the parameters of the wire electrical discharge machining process for composites made of Al6061 reinforced with nano-sized particles of both Sic and ZrO_2, which were produced through stir-casting. The addition of hybrid nano-powders to the aluminium matrix resulted in a durable material. Zirconia nanoparticles are highly effective at reinforcing aluminium matrices because of their physical, mechanical, and wear properties. This study explored the combined influence of 5 wt.% micro-/nano-SiC and different weight percentages (3, 6, 9) of nano-ZrO_2 on the tribology and mechanics of Al matrices fabricated using powder metallurgy.[20–22] Both pure Al and hybrid composites were subjected to wear surface analysis via SEM and statistical evaluation using ANOVA. Fayomi et al.[23] created a nano-hybrid material consisting of ZrB_2 and Si_3N_4 through a two-step liquid metallurgy process. The resulting material had different compositions, ranging from 0% to 20% in steps of 5 wt.%, reinforced in high-grade AA8011 to withstand the corrosive effects of aggressive environments, and could function as a thermally stable material suitable for use in automobiles.

Temperature changes can significantly affect the behaviour of composite materials. Depending on the specific type of composite material and its constituents, exposure to elevated temperatures can cause changes in its mechanical, thermal, and chemical properties. Researchers[24] successfully fabricated Aluminium6061-ZrO_2 MMCs using stir casting, observing a gradual increase in density and tensile strength with increasing ZrO_2 content (up to 6 wt.%). The 6 wt.% MMC exhibited the highest strength and improved wear resistance, though ductility decreased slightly.

Powder metallurgy offers several advantages, including producing complex shapes with high precision and uniformity and often without extensive machining. Additionally, it allows for incorporating various alloying elements and additives to achieve specific material properties.[25,26] Powder metallurgy is widely used in the automotive, aerospace, electronics, and healthcare industries to produce multiple components, from small intricate parts to large structural pieces.

Bharathi[27,28] investigated the mechanical hardness, compressive strength, and wear properties of Al7075 forfeited with SiC (2-6%) and B_4C(2 wt.%) using PM for automotive applications. The hardness of the hybrid composite decreased compared to the monolithic composite Al7075/SiC (6%) because of the addition of B_4C.

The study conducted by Yadav et al.[29] found that the hybrid aluminium nanocomposite reinforced SiC, ZrO_2, and Gr, i.e., at 3 wt.% with 1 wt.%, each exhibited the highest level of corrosion resistance when tested in a 3.5% NaCl solution at ambient temperature using the Tafel method.

Two different approaches were used to distinguish the corrosion rate of Al6061 alloy and its composites with reinforcements. The first approach involved using weight loss methods to test the materials in both acid and neutral chloride mediums. This approach allowed for the measurement of the mass lost by the materials due to corrosion. The second approach involved using electrochemical methods to measure the corrosion rate of the materials in the same acid and neutral chloride mediums. These methods allowed for a more precise measurement of the corrosion rate by analysing the materials' electrochemical behaviour during the corrosion process.[30,31]

The study[32] found that the addition of ZrO_2 nanoparticles (2,4,6 wt.%) in AA2024 significantly enhanced the corrosion resistance in a seawater environment. The findings revealed that the incorporating nanoscale zirconia containing 3, 6, 9, and 12 wt.% in LM-13 resulted in composites with superior corrosion resistance compared to the LM-13 alloy.[33] The study[34] found that increasing the weight percentage of TiC 10 to 20 wt.% in the AA8011 decreased the corrosion rate. However, adding graphite to 2 wt.% reduced the corrosion resistance of the composite.

Numerous studies have investigated the metal matrices reinforced with a combination of nanoceramic particulates (like ZrO_2 and SiC) and have consistently demonstrated that this is an effective method to improve their mechanical and wear properties. This research aims to engineer a novel nano-hybrid composite material by incorporating (ZrO_2+SiC) reinforcements within an AA6351 aluminium matrix. This composite material is envisioned to exhibit superior corrosion resistance in harsh environments while maintaining its structural integrity, ensuring longevity and reliability. Such characteristics make it a promising candidate for various applications in the marine and aerospace industries. AA6351/SiC/ZrO_2 composites offer a compelling material option in marine applications due to their synergistic properties as aluminium provides a lightweight matrix for improved fuel efficiency and SiC reinforcement enhances the composite's mechanical strength and wear resistance, which are crucial to withstanding the constant stress as well as friction in saltwater environments. Furthermore, ZrO_2 mitigates the inherent brittleness of SiC, improving fracture toughness and overall reliability. This combination balances desirable properties, including strength, wear resistance, and economic viability, making AA6351/SiC/ZrO_2 composites well suited for marine structures and components.

MATERIALS AND PROCESS

Composite Preparation

The research employed powders of silicon carbide, zirconium dioxide, and 6351 aluminium alloy, which were purchased from Nano Research Labs and Parshwamani Metals in India and Mumbai, respectively. The average particle size of the AA6351 powder, received from Parshwamani Metals in Mumbai, is 70-80 μm, while the particle sizes of SiC and ZrO_2 powders, received from Nano Research Lab in Jharkhand, India, are 30-50 nm each. Figure 1a-d presents the scanning electron microscopy and transmission electron microscopy images taken after receiving the particles. Using the powder metallurgy method, the researchers developed a combination of nanocomposites for analysis of AA6351-xSiC-$y$$ZrO_2$ (x = 5 wt.%; y = 0,3,6,9 wt.%).[35] Initially, an electronic weighing device (AS R220 plus, Switzerland) with a precision of 0.1 mg was utilized to measure the weight of the powders. Subsequently, a predefined quantity of particles was meticulously homogenized using a combination of mortar-pestle and planetary ball mill (VBCRC, Chennai), employing stainless-steel balls with 8-mm diameter and maintaining a ball-to-powder ratio of 10:1[36] to deter clustering of composite powders. During the blending process, the milling time was set at 20 min, and the speed was 125 rpm. The elemental composition of the milled blended powders was investigated using X-ray diffraction on a Bruker D8 instrument. The analysis aimed to identify all elements present in each blend by employing CuKα radiation (λ = 1.5418 Å) at 30 kV. The scan covered a significant angle range (20°-80°) with a fine step size (0.02°) to ensure comprehensive detection. After blending, green pellets measuring 13 mm in diameter and 5 mm in height were produced at a 3-tonne load for sintering in a muffle furnace (VBCRC, Chennai) using a 20-tonne automatic hydraulic pellet press (Fig. 2).[35] To ensure the efficient functioning of the die, the die wall was cleaned and lubricated with zinc stearate manually after each compaction procedure.

The green pellets were subjected to heating at 550°C for 1 h in a muffle furnace and then cooled to ambient temperature inside the furnace. The resulting sintered samples are shown in Fig. 3. The samples were mechanically polished and etched in Keller reagent for 10 s to prepare them for microstructural analysis.

Density and Porosity

The densities of all produced composites were assessed utilizing Archimedes' principle, a widely recognized technique renowned for its ease and precision in quantifying the volume of objects of any geometry as per ASTM B962-15 standards. A digital electronic weighing balance with a sensitivity of 0.01 mg was utilized to ensure utmost accuracy.

The principle is mathematically represented by Eq. 1:

$$\rho_{\mathrm{MMC}} = \frac{w_m}{(w_m - w_{m1})} * \rho_{\mathrm{water}} \tag{1}$$

where ρ_{MMC} is the density of the hybrid or non-hybrid composite; W_m and W_{m1} are the weights of sample in air and sample submerged in distilled water (ρ_{water} at 20°C is 0.998 g/cm^3).

The theoretical density of the composites is found using "rule of mixture" shown by Eq. 2.

$$\rho_{\mathrm{THMMC}} = W_{\mathrm{m}}\rho_{\mathrm{m}} + W_{r1}\rho_{r1} + W_{r2}\rho_{r2} \tag{2}$$

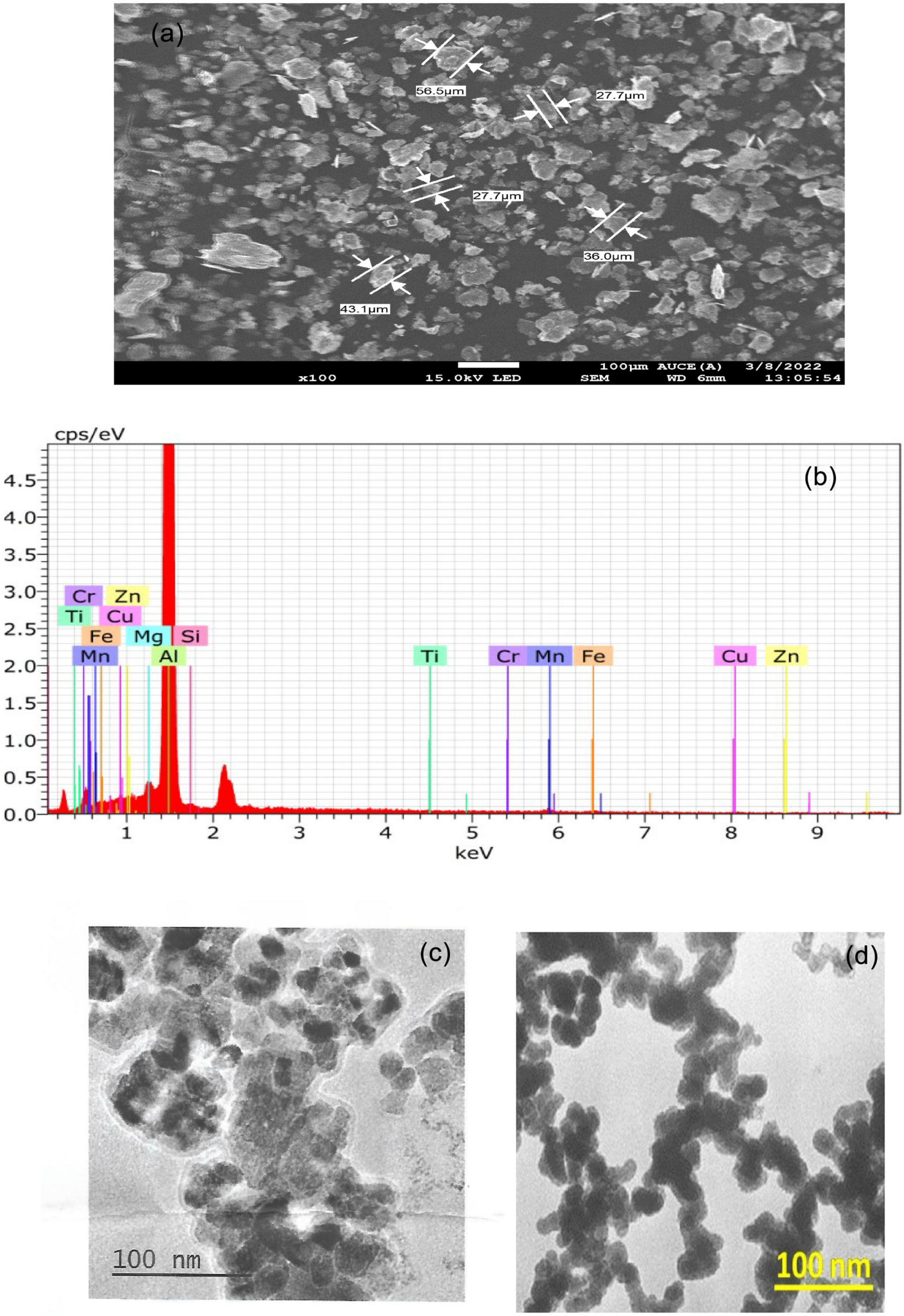

Fig. 1. Microstructure of (a) SEM of 6351 aluminium alloy particles; (b) elemental analysis of 6351 aluminium alloy; (c) TEM of nano-zirconia particles; (d) TEM of nano-SiC particles.

Fig. 2. Hydraulic pellet press.

$$\text{Porosity of the fabricated specimen } = \frac{\rho_t - \rho_e}{\rho_t} \quad (3)$$

Hardness and Relative Density Measurement

Hardness is a material's resistance against scratch, abrasion, or indentation. Assessing hardness often involves using methods like the Brinell, Rockwell, or Vickers tests, which are significant in materials testing. This study utilized the Micro Vickers hardness test machine, specifically the MATRIX model, following the ASTM E 384-22 standard procedure, to evaluate the hardness of composite materials with various compositions.

In the micro-Vickers hardness test, a standard rectangular pyramid diamond indenter creates impressions on the material surface under applied loads, typically 10 g to 1000 g. For this investigation, a load of 100 g was applied for a dwell time of 10 s. The indentation dimensions were determined using a microscope, and the hardness tester displayed the hardness values digitally.

Prior to testing, the material surface underwent preparation, including polishing with emery sheets of grades 600, 800, and 1000, followed by the application of Keller's agent. Three indentations were made on each sample to ensure accuracy in the experimental readings, and the average value was considered.

The hardness (HV) is determined using Eq. 4:

$$\mathrm{HV} = \frac{1854.4 * \mathrm{L}}{d_{\mathrm{avg}}^2} \quad (4)$$

Load L is measured in gram force, and d_{avg} (average diagonal) is in μm. HV can be converted to the unit of MPa and GPa by using two formulae: HV = HV × 9.807 MPa and HV = HV × 0.009807 GPa. However, normally HV is the standard value and used as a standard number for the demonstration of hardness value of a material.

Tafel Method

The electrochemical corrosion test was conducted on Vertex. C (IVIUM) workstation; aluminium alloys with a cross-sectional area of 1.0 cm^2 were used as the working electrodes. An electrode made of Ag/AgCl was utilized as a reference, while a thin platinum wire served as an auxiliary electrode in the test setup, as shown in Fig. 4. Prior to the corrosion test in the NaCl solution, all five samples were polished to a mirror-like polish using emery sheets of varying grades. The electrode configurations adhere to ASTM G 102 guidelines.[37] The corrosion current density, corrosion rate and corrosion potential are computed with a sweep rate of 10 mV/s and a potential range of -1 V to +1.5 V s at ambient temperature.

RESULTS AND DISCUSSION

Metallurgical Evaluation

XRD is commonly employed to identify distinct phases in materials by analysing their diffraction patterns compared to known reference patterns. The magnitude of the XRD peak acquired for a specific phase is contingent upon its proportion and dimensions within the material. X-ray diffraction (XRD) examination of the ball-milled powder samples ASZ2, ASZ3, ASZ4, and ASZ5 unveiled the presence of aluminium, silicon carbide (SiC), and zirconia (ZrO_2) phases as illustrated in Fig. 5a and b. The dominant peak confirms the presence of the aluminium of the AA6351 matrix. There are no observable peaks corresponding to the brittle phase Al_4C_3 in the XRD pattern. The composite fabricated was of 2θ ranging between 20° and 85°. The patterns matched well with reference data for SiC (COD-CIF 9010158),[38] aluminium (COD-CIF 1502689),[39] and ZrO_2 (COD-CIF 5000038).[40] The peaks at the 2θ angle confirm the presence of aluminium (JCPDS 04-0787) or PDF00-004-0787, ZrO_2 (JCPDS 37-1484) PDF 00-037-1484, and SiC (JCPDS:29-1129) PDF 00-029-1129. Peaks for Mg, Si, etc., related to Al6351 alloy were not detected because of low wt.% in the aluminium matrix.

X-ray diffraction peak analysis is a powerful tool for studying crystallite size and strain in materials. The Debye-Scherrer equation[41] calculates the average nanocrystalline size from the broadening of the peaks in the XRD pattern.

$$\mathrm{D} \;=\; \mathrm{k}\;\lambda\,/\,\beta_{\mathrm{hkl}}\cos\,\theta \quad (5)$$

where D is crystallite size, shape factor (k) = 0.90, λ = 1.5418°A, or 0.15418 nm; $\theta_{\text{ hkl}}$ is the Braggs angle and β_{hkl} full width half maximum.

Dislocation density (δ), representing the number of defects per unit volume within the crystals, is

Fig. 3. (a) Muffle furnace; (b) composite samples.

Fig. 4. Apparatus for polarization test.

used to quantify the defect concentration and is calculated using Eq. 6.

$$\delta = 1/\, D^2 \tag{6}$$

Figure 6 reveals a decreasing trend in crystallite size as the weight percentage (wt.%) of ZrO_2 reinforcement increases. It is attributed to the presence of hard ceramic SiC and ZrO_2, which promote matrix refinement. Moreover, these observations align with prior research,[42] indicating that the size of crystallites decreases as the percentage of reinforcement weight increases.

Energy-dispersive spectroscopy (EDS) confirmed the elemental composition of the samples, with peaks corresponding to aluminium, silicon, zirconium, magnesium, zinc, carbon, iron, oxygen, copper, and titanium detected, as shown in Fig. 7a and b.

Density and Porosity of HANMMC

Table I demonstrates that incorporating both SiC and ZrO_2 nanoparticles leads to a notable increase in the density of aluminium matrix composites. This observed enhancement is directly attributable to these reinforcements' inherently higher density than in 6351 aluminium alloy. However, porosity measurements based on theoretical and experimental densities reveal a contrasting trend.

Despite the observed density increase, porosity also exhibits a rising trend with the addition of SiC. The observed porosity increase is primarily linked to the intrinsic high hardness of SiC, which restricts the adequate compaction of the composite powder during processing. Similar observations of elevated porosity in Al/SiC composites have been reported in the literature.[5] Furthermore, introducing nano-ZrO_2 particles into the AA6351+5%SiC composite further exacerbates the porosity trend; these observations are primarily due to (1) the inherent propensity of nanoparticles to agglomerate, thereby hindering effective densification, and (2) the pronounced hardening effect exhibited by nanoparticles compared to their larger counterparts, which reduces the compressibility of the powder mixture and consequently leads to increased porosity.

Porosity is observed because of discrepancies in experimental and theoretical densities. However, the incorporation of nanoSiC and nanoZrO_2 particles as reinforcement materials into the aluminium matrix enhances the properties of AA6351 aluminium alloy by increasing the surface area.

Micro-Vickers Hardness and Relative Density

The quest for lightweight yet robust materials drives continued exploration of aluminium matrix composites (AMCs). This study investigates the efficacy of hybrid reinforcements in enhancing the hardness of sintered aluminium composites, explicitly focusing on the synergistic effects of SiC and ZrO_2 nanoparticles. Vickers hardness measurements, summarized in Table II, reveal a pronounced increase with the incorporation of reinforcements—SiC's 5 wt.% inclusion boosts hardness from 66 HV to 78 HV as a physical barrier to dislocation

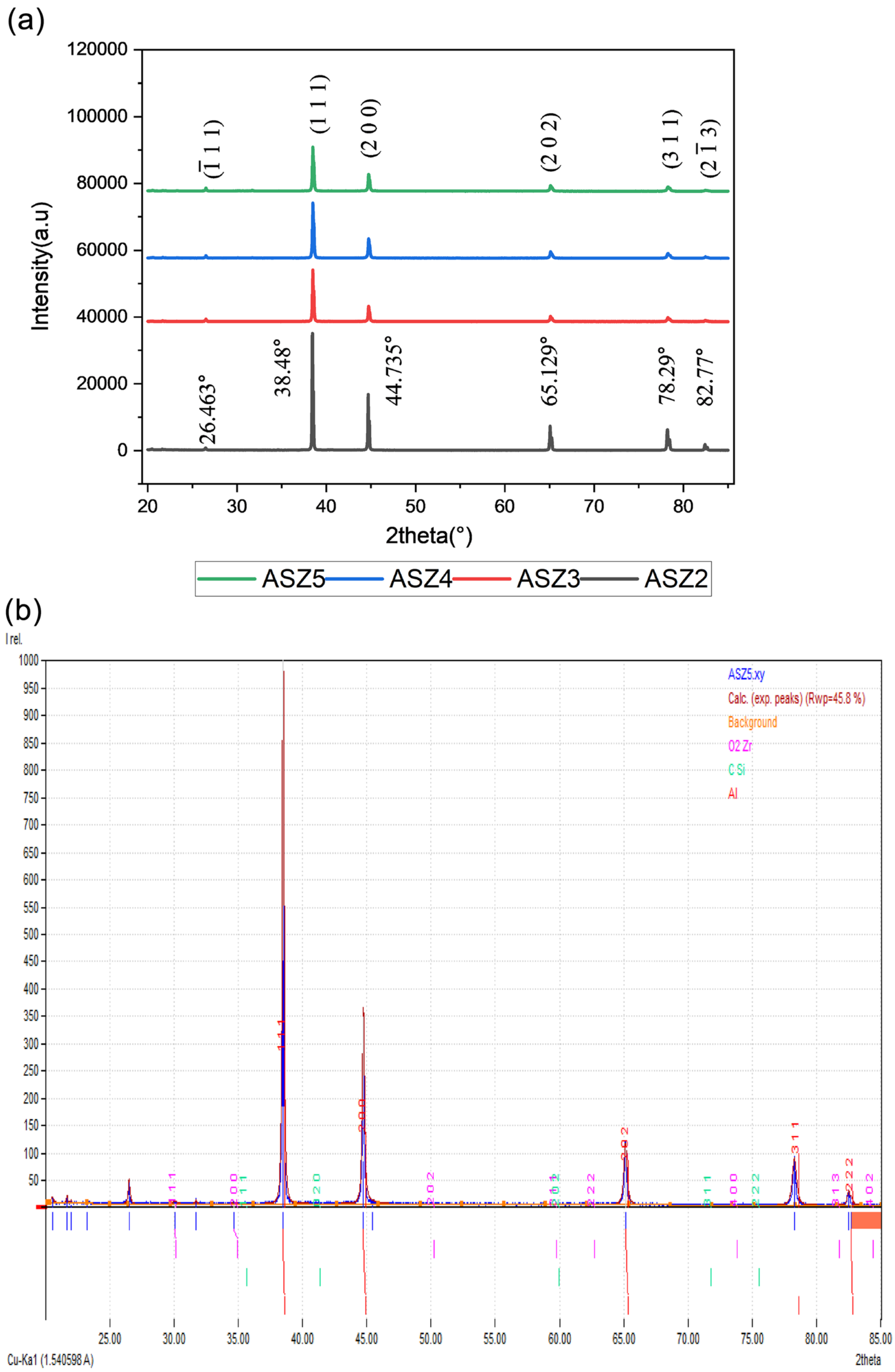

Fig. 5. (a) XRD samples (ASZ2, ASZ3, ASZ4 andASZ5). (b) XRD of SampleASZ5 - AA6351-SiC (5 wt.%)-ZrO_2 (9 wt.%).

movement. Further increments in ZrO_2 nanopowder (3 wt.% steps) within the AA6351+5%SiC matrix progressively enhance hardness due to

(1) Uniform distribution of both SiC and ZrO_2 throughout the composite microstructure;
(2) The high inherent density of ZrO_2 nanopowder contributing to a denser overall composite;
(3) Elevated intrinsic hardness of ZrO_2 nanoparticles compared to the aluminium matrix.

Overall, these findings align with previous studies,[20,21] indicating hybrid reinforcements, particularly SiC and ZrO_2 nanoparticles, demonstrate immense potential for tailoring and boosting the hardness of aluminium matrix composites.

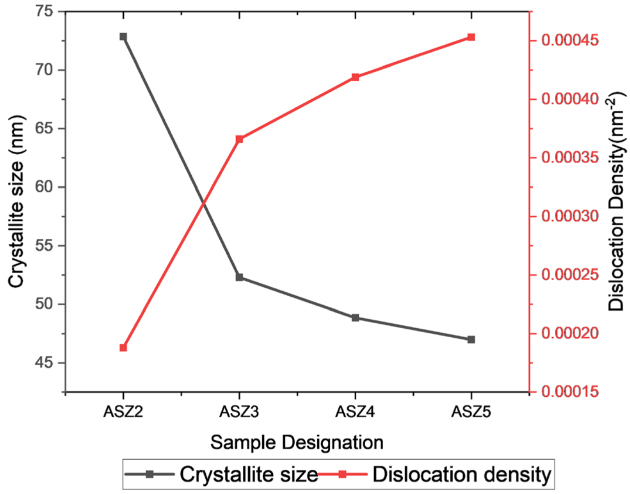

Fig. 6. Crystallite size and dislocation density of HANMMC around 38° XRD peak.

The relative density and hardness plots for Al6351+xSiC+yZrO$_2$ (where x = 5 and y = 0,3,6,9 wt.%) and pure Al6351 are shown in Fig. 8. The figure clearly illustrates that as the amount of nano-zirconia increases from 3 wt.% to 9 wt.%, the hardness of the composites rises while the relative density descends. Specifically, it is evident that with an addition of nanoSiC (5 wt.%), there is a notable decline in relative density. This decline can be attributed to the hard SiC particles resisting flattening during compaction, leading to the formation of inter-particle micro-voids. Moreover, the high-melting-point SiC particles tend to densely pack with a random distribution during sintering. Furthermore, adding nano-ZrO$_2$ in aluminium composites results in a decrease in relative density and an increase in Vickers hardness. This decline in relative density and elevation in hardness could be attributed to several factors: (1) conglomeration of nanoparticles at elevated concentrations; (2) the high hardness and density of nano-ZrO$_2$ particles hinder compaction.

The micro-Vickers hardness of sintered aluminium-based hybrid composites, incorporating 5 wt.% SiC into the aluminium matrix, resulted in a significant 18.18% increase in hardness, attributed to SiC's role in hindering dislocation movement. This can be due to the existence of hard ceramic SiC particles in the base alloy, reduced grain size, and the SiC particles acting as a hindrance to the motion of dislocation.[43] The increase in microhardness was due to the existence of a holding effect of the SiC particles and the Orowan strengthening mechanism. The incorporation of SiC particles formed a better grain structure and improvement in induced strain.[44] Subsequent addition of ZrO$_2$ nanopowder in incremental steps of 3 wt.% further augmented hardness. This increase may be due to nano-zirconia being ceramic, which is harder compared to matrix material. Hence, airconia acts as a load barrier and resists the deformation caused by indentation. Compaction pressure also plays a major role in increasing the hardness. This phenomenon of increase in the hardness with the addition of zirconia particles was also noticed by other researchers.[21]

Mechanism of Pitting Corrosion

Pitting corrosion is a localized form of corrosion that creates small holes or pits in the metal surface. It is an electrochemical process that can occur when aluminium is exposed to certain environments, such as saltwater or acidic ions. Electrochemical interactions drive corrosion in most metals at the boundary between the metal and a surrounding electrolyte solution. At the anode, the aluminium component loses electrons and dissolves into the electrolyte. The hydrolysis of Al^{3+} results in acidification at the pit's base, as illustrated by Eqs. 7 and 8. These released electrons travel through the composite to the cathode, where they typically trigger a reduction reaction with dissolved oxygen, forming hydroxide ions (Eq. 9). The dissolution of aluminium Al^{3+} ions at the bottom of the pit generates an electric field that attracts Cl$^-$ ions, forming AlCl$_4^-$ as depicted in Fig. 9.

Anodic reaction:

$$3\mathrm{Al} \rightarrow \mathrm{Al}^{3+} + 3e^- \tag{7}$$

$$\mathrm{Al}^{3+} + 3\mathrm{H_2O} \rightarrow \mathrm{Al\,(OH)_3} + 3\mathrm{H}^+ \tag{8}$$

Cathodic reaction:

$$\mathrm{O_2} + 2\mathrm{H_2O} + 4e^- \rightarrow 4\,\mathrm{OH}^- \tag{9}$$

As Al (OH)$_3$ accumulates, it creates a dome over the pit's surface, gradually obstructing the pit opening. This obstruction can impede the exchange of Cl$^-$ ions, potentially slowing down or stopping pit growth. Consequently, a corrosion pit can be seen as a local anode surrounded by a cathodic matrix. Once pitting corrosion begins, pit growth can continue at lower potentials than the initial pitting potential. The rate of corrosion is directly proportional to the current flowing within this miniature electrochemical cell the faster the aluminium dissolves, indicating a more rapid corrosion rate. Notably, there's a specific potential where the rate of metal dissolution is balanced by the rate of hydrogen evolution. This specific potential and its corresponding current density represent the material's inherent corrosion rate, which can be analysed using a Tafel plot.

Calculation of Rate of Corrosion

To produce the Tafel curves, the logarithm of the corrosion current density was plotted against the potential. The slopes of the linear areas are represented by the Tafel constants βa and βc. To create E$_{corr}$, these linear zones are extended until they

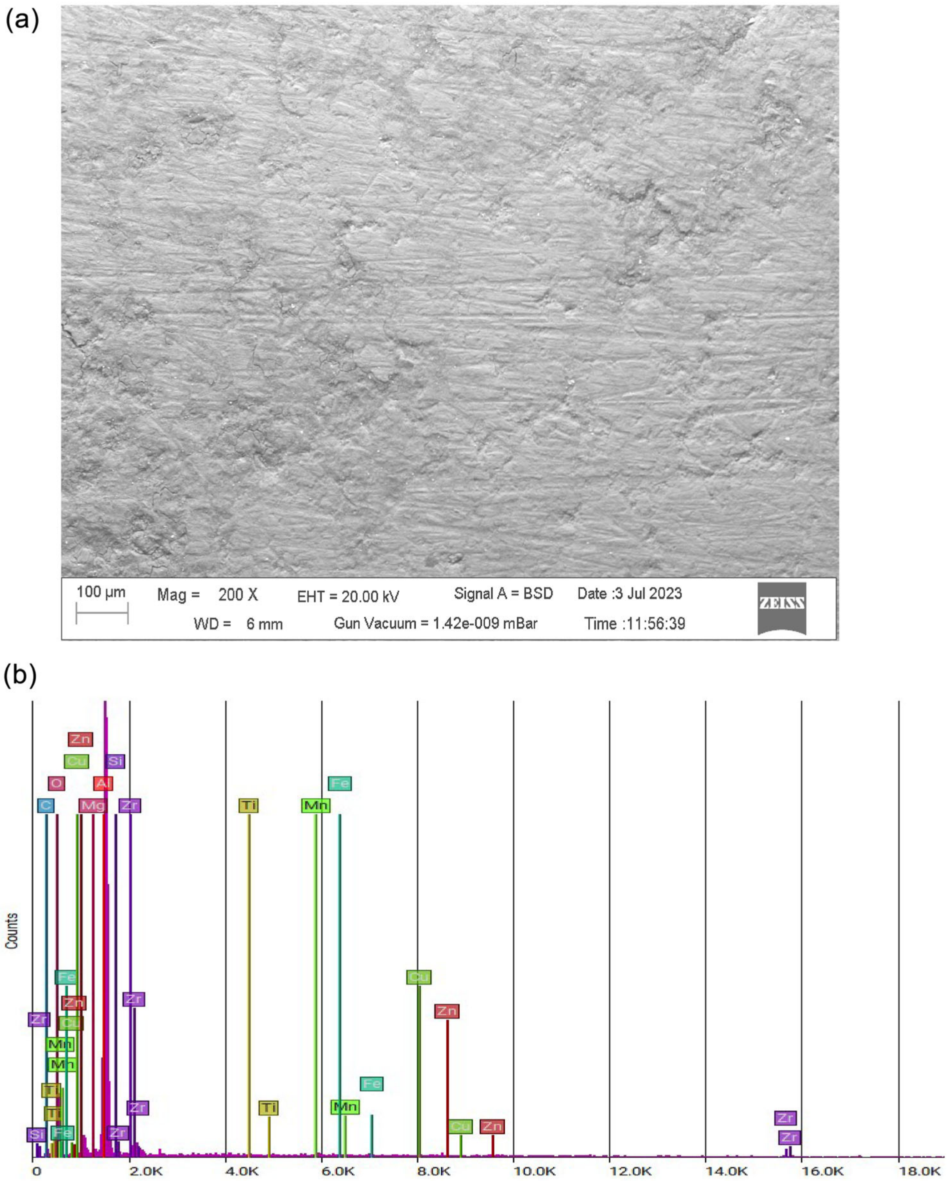

Fig. 7. (a) SEM of Al6351 + + 5%SiC + 9% ZrO_2 hybrid nano-metal matrix composites. (b) EDS spectrum of Al6351 + + 5%SiC + 9% ZrO_2 hybrid nano-metal matrix composites.

Table I. Theoretical density and porosity of AA6351 and HANMMC

Sample designation	Theoretical density, g cm^{-3}	Experimental density, g cm^{-3}	Porosity, %
ASZ1	2.70	2.687	0.48148
ASZ2	2.72	2.695	0.91911
ASZ3	2.7655	2.7116	1.94901
ASZ4	2.8108	2.7248	3.05962
ASZ5	2.8571	2.7408	4.07056

intersect.[31] The log I_{corr} values at the intersection of the coordinates give the corrosion current density. Tafel polarisation curves of the five samples are depicted in Fig. 10. Table III displays the corrosion rate for the five samples in 3.5% NaCl, computed using Eq. 10.

$$\text{CoR} = \frac{K_1 \times \text{Equivalent Weight} \times I_{\text{corr}}}{\rho} \tag{10}$$

Table II. Average micro-Vickers hardness

Sample designation	Trial 1 Davg, μm	Trial 1 Hardness value	Trial 2 Davg, μm	Trial 2 Hardness value	Trial 3 Davg, μm	Trial 3 Hardness value	Average hardness, HV
ASZ1	56.22	59	49.33	76.2	54.4	62.7	66
ASZ2	51.72	69	49.33	76.2	45.7	88.8	78
ASZ3	44.46	93.8	47.04	83.8	41.21	109.2	95.6
ASZ4	39.2	120.7	39.77	117.2	39.01	121.9	119.9
ASZ5	37.76	130	35.37	148.2	34.61	154.8	144.3

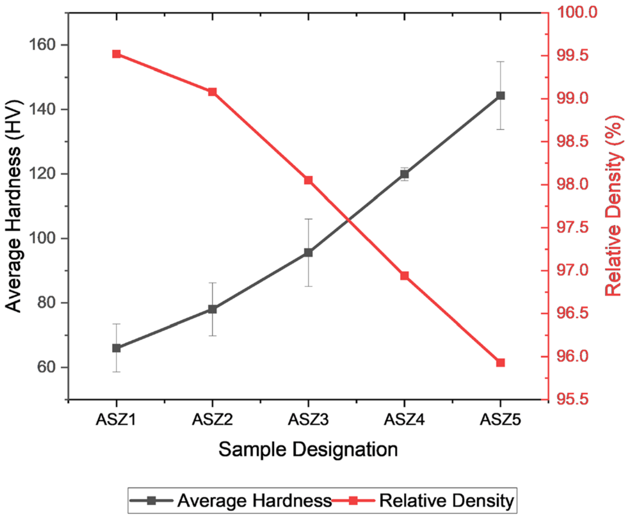

Fig. 8. Hardness and relative density of AA6351 and HANMMC.

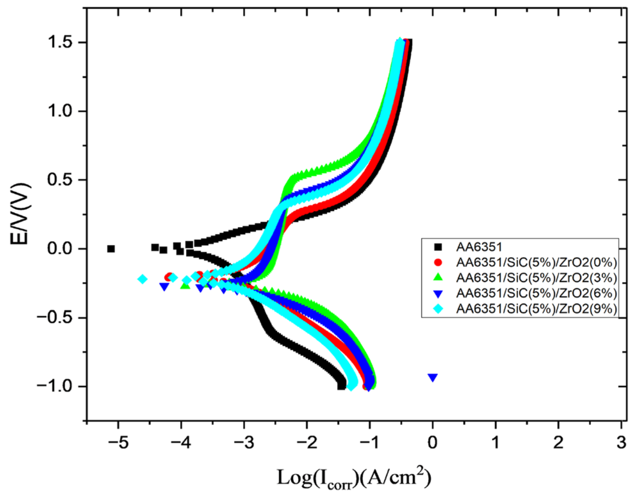

Fig. 10. Tafel polarisation curves of AA6351 and HANMMC.

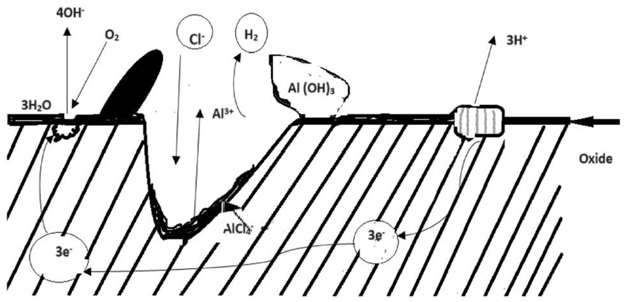

Fig. 9. Mechanism of pitting corrosion.

where CoR represents the rate of corrosion in millimetres per year, Icorr denotes the corrosion current density in microamperes per square centimetre (μA/cm^2), which is the ratio of the corrosion current (i_{corr}) to the sample area (1 cm^2), and ρ stands for the density of the samples in grams per cubic centimetre (g/cm^3). The constant K1 is equal to 3.27×10^{-3} mm g/μA cm year. The sample's equivalent weight is measured in grams.

Table III presents the corrosion rate for AA 6351 and its hybrid aluminium nanocomposites in a 3.5% NaCl solution, calculated using the Eq. 7 above.[35] The Tafel curves demonstrate that a hybrid composite's corrosion rate descends as the weight percentage of nano-zirconia accelerates. Compared to 3 wt.% nanoZrO_2, the hybrid composite's Tafel plot at 9 wt.% nanoZrO_2 exhibits the steepest anodic slope and I_{corr} current; hence, it is corrosion resistant. This illustrates that with the increase of nano-ZrO_2 from 3 wt.% to 9 wt.% in the AA6351/SiC, the corrosion rate descends from 0.6533 mm/year to 0.1873 mm/year. Zirconia and SiC are inert ceramic particles that the corrosion may scarcely impact, which may explain the enhanced corrosion resistance. When ZrO_2 nanoparticles are dispersed within the alloy matrix, they act as physical barriers. These particles block the pathways that corrosive agents, such as moisture and ions, would typically use to penetrate the material. By obstructing these pathways, the ZrO_2 reinforcement helps to locally protect the metallic surface from exposure to the corrosive environment. Refs. 32 and 33 observed similar results in Al2024 composites and LM-13 reinforced with nano-zirconia particles and observed an increase in corrosion resistance with an increase in reinforcement content. The inert ceramic particles occupy a portion of the surface area, effectively reducing the exposed metal

Table III. Sample rate of corrosion

Sample designation of composites	Slope (V/dec) Anodic	Slope (V/dec) Cathodic	I_{corr}(A/cm^2)	E_{Corr} (V)	Rate of corrosion (mm/year)
ASZ1	0.091	0.118	7.323E−06	0.0048	0.08067
ASZ2	0.212	0.171	0.00003994	−0.2076	0.4399
ASZ3	0.202	0.064	0.00005931	−0.1509	0.6533
ASZ4	0.133	0.056	0.00003495	−0.2819	0.385
ASZ5	0.127	0.097	0.00001701	−0.2213	0.1873

surface available for corrosion, leading to a lower overall corrosion rate.

CONCLUSIONS

Hybrid AA6351 composites containing 5% SiC and varying amounts of ZrO_2 (0-9%) were manufactured via powder metallurgy. Both mechanical and corrosion properties were evaluated. Key findings include:

- SEM-EDS and XRD confirmed successful composite synthesis.
- Reinforced particles were reasonably well distributed within the matrix.
- Hardness significantly increased with nanoSiC and nanoZrO_2 content, exceeding that of pure aluminium.
- Electrochemical methods such as Tafel extrapolation proved to be effective in evaluating the corrosion behaviour of composite materials.
- The incorporation of nanosized silicon carbide (SiC) and zirconium oxide (ZrO_2) into the AA6351 matrix led to a substantial improvement in the composite's resistance to corrosion.
- The composite containing highest amount of zirconia nanoparticles (9 wt.%) and silicon carbide nanoparticles of 5 wt.% is best in terms of hardness (144.3 HV) and corrosion rate (0.1873 mm/year) for the HANMMC.
- Corrosion resistance increases with the zirconia content in the nanohybrid metal matrix composites. Samples are ranked in descending order of resistance: ASZ5 > ASZ4 > ASZ3; incorporating a higher weight percentage of zirconia enhances the composite's ability to withstand corrosion.

Overall, this study's results suggest that using nano-hybrid reinforcements in aluminium matrix composites can improve properties, including enhanced corrosion resistance. These discoveries carry significant ramifications for advancing novel composite materials suited for applications in maritime and aeronautical domains.

ACKNOWLEDGEMENT

The authors thank GITAM Deemed University Visakhapatnam, Department of Mechanical Engineering, for providing the experimental facility. The authors thank the Central Instrumentation facility, Savitribai Phule Pune University, Pune and Murti facilities, GITAM, for providing FESEM/EDS facility to carry out the experimental work.

AUTHOR CONTRIBUTIONS

All authors contributed to the study conception and design. Material preparation, data collection and analysis were performed by Sr. Prof. Dr. K.Venkatasubbaiah and T. Sarithnaidu. The first draft of the manuscript was written by T. Sarithnaidu, and all authors commented on previous versions of the manuscript. All authors read and approved the final manuscript.

FUNDING

The authors declare that no funds, grants, or other support were received during the preparation of this manuscript.

DATA AVAILABILITY

All data used to support the findings of this study are included within the article.

CONFLICT OF INTEREST

The authors declare that they have no conflict of interest. The authors have no relevant financial or non-financial interests to disclose.

CONSENT FOR PUBLICATION

The authors declare that the figures and tables used in this manuscript are original and are not published anywhere else.

REFERENCES

1. T.G. Rambau, A.P.I. Popoola, C.A. Loto, T. Mathebula, and M. Theron, *Int. J. Electrochem. Sci.* 8, 5515 (2013).
2. P. Sharma, S. Sharma, and K. Dinesh, *J. Asian Ceram. Soc.* 3, 240 (2015).
3. P.C. McDonald, E. Jaramillo, and B. Baudouy, *Cryogenics* 46, 298 (2006).

4. B. Baudouy and A. Four, *Cryogenics* 60, 1–4 https://doi.org/10.1016/j.cryogenics.2013.12.008 (2014).
5. O. El-Kady and A. Fathy, *Mater. Design* 54, 348 https://doi.org/10.1016/j.matdes.2013.08.049 (2014).
6. K. Sekar, G. Jayachandra, and S. Aravindan, *Mater. Today Proc.* 5, 20268 (2018).
7. P.S.R. Kumar, D.R. Smart, and S.J. Alexis, *J. Asian Ceram. Soc.* 5, 71 (2017).
8. A. Baradeswaran and A.E. Perumal, *Compos. Part B Eng.* 56, 464 (2014).
9. A. Baradeshwaran, S.C. Vettivel, A.E. Perumal, N. Selvakumar, and R.F. Issac, *Mater. Des.* 63, 620 (2014).
10. K.S. Shetty and A.N. Shetty, *Surf. Eng. Appl. Electrochem.* 51, 374 (2015).
11. S. Arif, M.T. Alam, T. Aziz, and A.H. Ansari, *Mater. Res. Express* 5(4), 046534 https://doi.org/10.1088/2053-1591/aabcf0 (2018).
12. A.H. Karabacak, A. Çanakçı, and F. Erdemir, *SILICON* 14, 8567 https://doi.org/10.1007/s12633-021-01582-7 (2022).
13. S. Kumar, A. Kumar, and C. Vanitha, *Mater. Today Proc.* 15, 21 https://doi.org/10.1016/j.matpr.2019.05.019 (2019).
14. E.S.M. Sherif, H.S. Abdo, K.A. Khalil, and A.M. Nabawy, *Int. J. Electrochem. Sci.* https://doi.org/10.20964/2016.06.18 (2016).
15. R. Sharma, A.K. Singh, A. Arora, S. Pati, and P.S. De, *Trans. Nonferrous Met. Soc. China* 29(7), 1383 https://doi.org/10.1016/S1003-6 (2019).
16. M.B.N. Shaikh, S. Arif, and M.A. Siddiqui, *Mater. Res. Express* 5, 046506 (2018).
17. S. Arif, T. Aziz, and A.H. Ansari, *Mater. Focus* 7(6), 901 https://doi.org/10.1166/mat.2018.1612 (2018).
18. T. Aoshuang, T. Jie, Z. Xiang, F. Dingfa, and Z. Hui, *Powder Metall.* 60, 66 (2017).
19. C. Thiagarajan, T. Maridurai, T. Shaafi, and A. Muniappan, *Mater. Today: Proc.* https://doi.org/10.1016/j.matpr.2021.07.029 (2023).
20. A. Khan, M.W. Abdelrazeq, M.R. Mattli, M.M. Yusuf, A. Alashraf, P.R. Matli, and R.A. Shakoor, *Crystals* 10, 904 https://doi.org/10.3390/cryst10100904 (2020).
21. S. Arif, M.T. Alam, A.H. Ansari, M.A. Siddiqui, and M. Mohsin, *Mater. Res. Express* 4, 076511 https://doi.org/10.1088/2053-1591/aa7b5f (2017).
22. S. Arif, M.T. Alam, A.H. Ansari, M.B.N. Shaikh, and M.A. Siddiqui, *Mater. Res. Express* 5, 056506 https://doi.org/10.1088/2053-1591/aabec8 (2018).
23. J. Fayomi, A.P.I. Popoola, and O.M. Popoola, *Mater. Res. Express*. https://doi.org/10.1088/2053-1591/ab4fd0 (2019).
24. G.V. Kumar, R. Pramod, C.G. Sekhar, G.P. Kumar, and T. Bhanumurthy, *Heliyon*. https://doi.org/10.1016/j.heliyon.2019.e02858 (2019).
25. D. Dey, A. Bhowmik, and A. Biswas, *SILICON* 14, 1 https://doi.org/10.1007/s12633-020-00757-y (2022).
26. M.S. Surya, *SILICON* 14(6), 2731 https://doi.org/10.1007/s12633-021-01053-z (2022).
27. P. Bharathi and T.S. Kumar, *SILICON*. https://doi.org/10.1007/s12633-023-02347-0 (2023).
28. P. Bharathi and T. Sampath Kumar, *SILICON*. https://doi.org/10.1007/s12633-023-02498-0 (2023).
29. S. Yadav, S. Gangwar, P.C. Yadav, V.K. Pathak, and S. Sahu, *Surface Topogr.: Metrol. Prop.* 9, 045022 https://doi.org/10.1088/2051-672X/ac2f87 (2021).
30. J.A. Kamaj, *Asian J Appl Sci* 3, 264 (2015).
31. N. Sunitha, K.G. Manjunatha, S. Khan, and M. Sravanthi, *SN Appl. Sci.* 1, 1024 https://doi.org/10.1007/s42452-019-1063-6 (2019).
32. E. Kennedy, B.S. Sachin, M. Ramachandra, C.A. Niranjan, N. Sriraman, V.K.S. Jain, and N.S. Narayanan, *Mater. Today: Proc.* https://doi.org/10.1016/j.matpr.2020.06.194 (2021).
33. J. Hemanth and M.R. Divya, *J. Mater. Sci. Chem. Eng.* 6(7), 136 https://doi.org/10.4236/msce.2018.67015 (2018).
34. A. Karthikeyan and G.R. Jinu, *Mater. Res. Express* 6, 1065b5 https://doi.org/10.1088/2053-1591/ab3e87 (2019).
35. T. SarithNaidu and K. Venkata Subbaiah, *J. Inst. Eng. India Ser. D*. https://doi.org/10.1007/s40033-023-00567-7 (2023).
36. H. Abbasi, M. Zeraati, R.F. Moghaddam, N.P.S. Chauhan, G. Sargazi, and R. Di Lorenzo, *Materials* 15(23), 8593 https://doi.org/10.3390/ma15238593 (2022).
37. ASTM G102: Practice for Calculation of Corrosion Rates and Related Information from Electrochemical Measurements.
38. C.L. Burdick and E.A. Owen, *Am. Chem. Soc.* 40(12), 1749 https://doi.org/10.1021/ja02245a001 (1918).
39. F.M. Mulder, B. Assfour, J. Huot, T.J. Dingemans, M. Wagemaker, and A.J. Ramirez-Cuesta, *J. Phys. Chem. C* 114, 10648 (2010).
40. U. Martin, H. Boysen, and F. Frey, *Acta Cryst.* B49, 403 https://doi.org/10.1107/S0108768192011297 (1993).
41. B.D. Cullity, *Elements of X-Ray Diffraction*, 2nd edn. (Addison-Wesley Publishing Company Inc., Phillippines, 1978).
42. K. Pal, K. Navin, and R. Kurchania, *Mater. Today: Proc.* https://doi.org/10.1016/j.matpr.2020.02.570 (2020).
43. M. Ali and S. Mohsen Ostad, *Trans. Nonferrous Met. Soc. China* 22, 275 (2012).
44. A. Devaraju, A. Kumar, A. Kumaraswamy, and B. Kotiveerachari, *Mater. Des.* 51, 331 (2013).